On the Use of Ray Tracing for Performance Prediction of UWB Indoor Localization Systems

Paul Meissner[1], Mingming Gan[2], Francesco Mani[3], Erik Leitinger[1],
Claude Oestges[4], Thomas Zemen[2], and Klaus Witrisal[1]
[1]Graz University of Technology, Austria; [2]FTW Forschungszentrum Telekommunikation Wien, Austria;
[3]COMELEC Department, Telecom ParisTech, France; [4]ICTEAM, Université catholique de Louvain, Belgium

***Abstract*—The most important factors impairing the performance of radio-based indoor localization systems are propagation effects like strong reflections or diffuse scattering. To the full extent, these effects can be captured only by time-consuming measurement campaigns. Ray tracing (RT) offers the possibility to predict the radio channel for a certain environment, avoiding the need for measurements. However, it is crucial to include all relevant propagation mechanisms in the RT as well as to validate the obtained results. In this paper, we show that sub-band divided RT can yield realistic ultra-wideband channel impulse responses that can be used instead of real measurements. We show this by using the RT results for performance prediction of multipath-assisted localization, which depends to a great extent on the above mentioned propagation effects. A previously introduced method to estimate the ratio of the signal energies of deterministically reflected paths to diffuse scattered components is employed on both the RT results and the channel measurements in an indoor environment. This analysis is useful in two ways: first, as this ratio scales the amount of position-related information of deterministic multipath components, it can be used for localization performance prediction; second, this ratio includes two main propagation mechanisms and is thus useful to validate the sub-band divided RT.**

I. Introduction

The performance of indoor localization systems based on radio signals is strongly affected by the propagation channel. Non line-of-sight (NLOS) situations between anchor nodes and the user terminal can cause large biases in range or angle estimation. Channel measurements can help to predict the expectable accuracy in a certain environment, either by using them for modeling the ranging error [1] or to evaluate parametrized performance bounds [2], [3]. However, such measurement campaigns are usually time-consuming and tedious to perform.

An available floor plan of the indoor environment offers several benefits for indoor localization. First, it allows for multipath-assisted indoor navigation and tracking (MINT), which maps reflected multipath-components (MPCs) to virtual anchors, i.e. mirror images of the physical anchor nodes with respect to reflecting surfaces like walls [2], [3]. In this way, it makes use of the geometric structure of MPCs [4], exploiting more information in the received signal than just the direct path. Second, together with electric properties of the building materials, the floor plan can be used for ray tracing (RT) simulations. With RT, realistic channel impulse responses can be obtained [5]. Some RT tools can also provide diffuse multipath (DM) contributions, which aim to model the non-coherent part of the channel. This DM can be very pronounced in indoor environments and can impair localization performance.

The evaluation of the usefulness of signals generated by RT for localization is not trivial. In references like [5], power delay profiles (PDPs) over some geometric areas are used. The large density of specular paths and the averaging process cause PDPs that nicely fit to measured ones. However, for individual signals, the degree of realism in terms of the different propagation mechanisms is unclear. By evaluating the usefulness of a sub-band divided RT tool for the purpose of performance prediction of the MINT approach, the following contributions to this problem are made in this paper:

- The quantification of position-related information of MPCs requires the estimation of the energy ratio of deterministic MPCs and DM. This allows for detailed local evaluation of propagation effects modeled by RT.
- It is shown that despite some limitations, RT can provide reasonable predictions of the localization performance without the need for tedious measurement campaigns.
- Insight is given on important future research directions that allow RT tools to produce more realistic signals.

The paper is organized as follows: Section II introduces the signal models and the measurement environment, in Section III, the RT tool and its configuration are described. The extraction of performance parameters is described in Section IV and Section V discusses the results.

II. Scenario, Measurements, and Signal Model

The scenario used for both RT and the measurement campaign is illustrated in Fig. 1, while geometry and building materials are described in Sec. III-C. Fig. 1b shows the locations of transmitter (Tx) and receiver (Rx) antennas. The latter form a grid of 22 x 22 points, spaced by $5\,\mathrm{cm}$, covering an area of roughly $1\,\mathrm{m}^2$. In an indoor localization application, the Tx is usually an anchor node at a known location. For the

The work of P. Meissner, E. Leitinger and K. Witrisal was partly supported by the Austrian Science Fund (FWF) within the National Research Network SISE project S10610, and by the Austria Research Promotion Agency (FFG) within KIRAS PL3, grant nb. 832335 “LOBSTER”.
The work of M. Gan and T. Zemen is supported by the Austrian Science Fund (FWF) through grant NFN SISE (S10607) and by the Austrian Competence Center FTW Forschungszentrum Telekommunikation Wien GmbH within project I0. FTW is funded within the program COMET - Competence Centers for Excellent Technologies by BMVIT, BMWFJ, and the City of Vienna. The COMET program is managed by the FFG.

ray tracing simulations, the middle horizontal line of the grid, marked in blue in Fig. 1b, is used. The UWB channel has been measured using a Rhode & Schwarz ZVA-24 vector network analyzer (VNA) at 7501 frequency points over the frequency range from 3.1 to 10.6 GHz.

Using a transmitted pulse $s(\tau)$, the received signal at the ℓ-th Rx position $\mathbf{p}_\ell$ is modeled as [2], [3]

$$r_\ell(\tau) = \sum_{k=1}^{K_\ell} \alpha_{k,\ell} s(\tau - \tau_{k,\ell}) + s(\tau) * \nu_\ell(\tau) + w_\ell(\tau). \quad (1)$$

Here, $\alpha_{k,\ell}$ and $\tau_{k,\ell}$ denote the complex amplitude and the propagation delay of the k-th deterministic, i.e. specular reflected, MPC. The number K_ℓ of deterministic MPCs varies with the position. The noise term $w_\ell(\tau)$ is white Gaussian measurement noise with two-sided PSD $N_0/2$, whereas $\nu_\ell(\tau)$ denotes a random process modeling the DM, filtered by the transmit pulse. We assume that the delays can be modeled geometrically using virtual transmitters (or anchors), which are mirror images of the anchor node with respect to reflecting surfaces, given in a floor plan of the environment. The positions of these virtual anchors (VAs) are denoted as $\mathbf{a}_k$, resulting in $\tau_{k,\ell} = \frac{1}{c}||\mathbf{p}_\ell - \mathbf{a}_k||$ for the corresponding delay, where c is the speed of light. Fig. 1b shows the positions of several VAs.

Both the RT and the measured signals are pulse-shaped with $s(\tau)$, a raised-cosine pulse with pulse duration T_p and roll-off factor β_R. This is done to select a desired frequency band for the analysis and to facilitate a search-and-substract MPC estimation algorithm. At position $\mathbf{p}_\ell$, the set of expected delays to the visible VAs can be computed using ray tracing. Using an algorithm described in Section IV, estimates $\hat{\alpha}_{k,\ell}$ and $\hat{\tau}_{k,\ell}$ of the corresponding complex amplitudes and delays are obtained. Assuming negligible noise $w_\ell(\tau)$, this yields an estimate of the deterministic and the diffuse part of the channel [6]

$$\hat{\nu}_\ell(\tau) = r_\ell(\tau) - \hat{r}_{\ell,\text{det}}(\tau) = r_\ell(\tau) \sum_{k=1}^{K_\ell} \hat{\alpha}_{k,\ell} s(\tau - \hat{\tau}_{k,\ell}) \quad (2)$$

Evaluating (2) at all measurement positions, local power delay profiles (PDPs) of the both received signal and the diffuse parts can be estimated. For a center point $\mathbf{p}_{\bar{\ell}}$, the PDP is defined as the expectation with respect to the position of instantaneous PDPs around $\mathbf{p}_{\bar{\ell}}$. Using the L spatially closest points around $\mathbf{p}_{\bar{\ell}}$, defined as the set $\mathcal{P}_{\bar{\ell}}$, an estimate of the local PDP of the DM is obtained as

$$S_{\nu,\bar{\ell}}(\tau) = E_{\mathbf{p}_\ell}\{|\nu_\ell(\tau)|^2\} \approx \frac{1}{L} \sum_{\mathbf{p}_\ell \in \mathcal{P}_{\bar{\ell}}} |\hat{\nu}_\ell(\tau)|^2. \quad (3)$$

Prior to the averaging operation, the LOS propagation delay is removed from the signals.

III. RT Analysis

RT is a deterministic propagation prediction tool, which has been widely used to simulate indoor channel characteristics for both narrowband and wideband systems. Due to the frequency selective properties of the propagation channel, the channel characteristics may vary significantly within the entire bandwidth of an ultra-wideband (UWB) system. Therefore, a conventional RT implementation at one discrete frequency point, used for narrowband systems, is not sufficient to simulate UWB channels. The usual way to overcome this problem is to use a sub-band divided RT algorithm [7], [8].

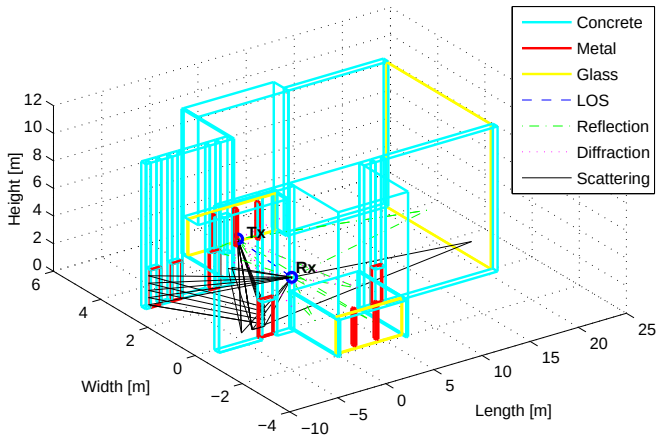

(a)

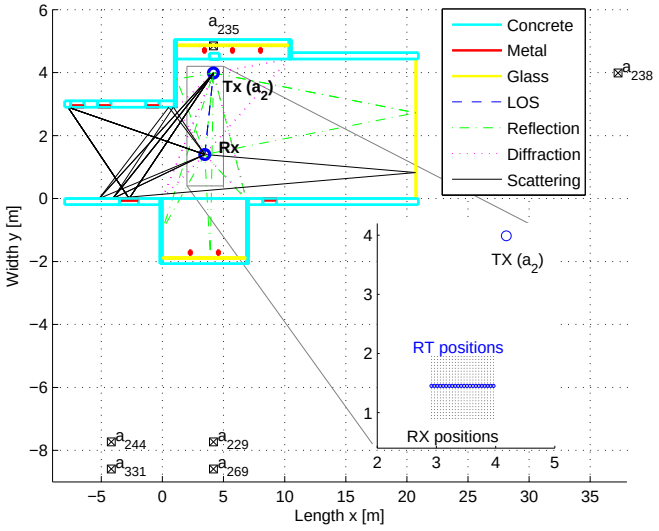

(b)

Fig. 1. Pictorial view of the RT constructed scenario considering one selected Rx position from the grid. (a) 3-D view. (b) 2-D view, also showing a close-up view of the measurement grid positions together with the positions where ray tracing simulations are available. The 2-D plot also shows the locations $\mathbf{a}_i$ of the virtual anchors that are analyzed in Section V.

A. Conventional RT

The RT algorithm employed in the present work is three-dimensional (3D) and requires the thorough geometrical and electromagnetic description of the indoor scenario, as well as the radiation properties of the antennas. The propagation mechanisms taken into account are: line-of-sight (LOS), reflection, penetration, diffraction and diffuse scattering. The

complex dyadic reflection and penetration coefficients are calculated applying Fresnel formulas [9], while diffraction is implemented using the uniform theory of diffraction (UTD) [10]. The diffuse scattering components aim to model the non-specular part of the channel. The diffuseness can be created in RT by dividing the surfaces into multiple tiles, whose size is determined by recursively dividing the surface until the far field condition is satisfied [11]. A directive scattering pattern model, which assumes that the scattering lobe is steered towards the direction of the specular reflection [12], is used to evaluate the amplitude of the diffuse scattering field. Moreover, based on the assumption that the diffuse scattering rays are incoherent, a uniformly distributed random phase is associated with each diffuse scattering ray [13].

B. Sub-band Divided RT

Applying a sub-band divided RT algorithm to UWB radio channels has already been proposed in [7], [8]. The basic concept is simulating the propagation channels at multiple frequency points, which are the center frequencies of the corresponding sub-bands. It is evident that the accuracy of the sub-band divided RT is related to the number of the sub-bands: the larger this number the better the accuracy, but at the cost of an higher computational effort. Sub-band divided RT can be summarized with the following steps [7], [14]:

- The whole UWB bandwidth is divided into several sub-bands. In each sub-band, constant frequency characteristics can be assumed for all materials and mechanisms.
- Conventional RT is used to obtain the channel impulse response (CIR) at each sub-band center frequency.
- The sub-band frequency responses are calculated by Fourier transforms. Afterwards all frequency responses over different sub-bands are combined into a complete frequency response over the whole UWB bandwidth.
- Finally, the CIR over the entire UWB bandwidth can be obtained by an inverse Fourier transform.

The complete frequency response can be expressed as:

$$H(f) = \sum_{i=1}^{N} \mathcal{F}\{h_i(\tau)\} \cdot R_i(f), \tag{4}$$

where i is the sub-band index, N is the total number of sub-bands, $\mathcal{F}\{\cdot\}$ is the Fourier transform, $h_i(\tau)$ is the CIR at the $i-$th sub-band, and $R_i(f)$ is the rectangular window function associated with the $i-$th sub-band. The complete frequency response $H(f)$ can be compared to the raw measurement data obtained from the VNA. In the following sections, we will use either the complete frequency response $H(f)$ or the measured channel frequency response to do the subsequent analysis.

C. Simulation Configuration

According to the measurement environment, the simulated scenario is built as shown in Fig. 1, where only one Rx position is shown as an example. The size of the simulated indoor scenario is about 29m $\times$ 7.1m $\times$ 10.5m. The blocks, including doors, walls and pillars, are made of different materials, such as concrete, metal and glass. A metallic block is considered as a perfect electric conductor (PEC). The values of relative permittivity ε_r and conductivity σ of other materials are: $\varepsilon_r = 6$ and $\sigma = 0.08$ S/m for concrete blocks, and $\varepsilon_r = 5.5$ and $\sigma = 0$ S/m for glass blocks. Since it is difficult to distinguish how the dielectric properties vary with the frequencies, we assume that the dielectric properties in the present work are independent of the frequency within the entire bandwidth of interest. In our simulation, the frequency bandwidth of 7.5 GHz is divided into $N = 15$ sub-bands with 500 MHz each. The transmitting and receiving antennas are assumed to be omnidirectional dipoles.

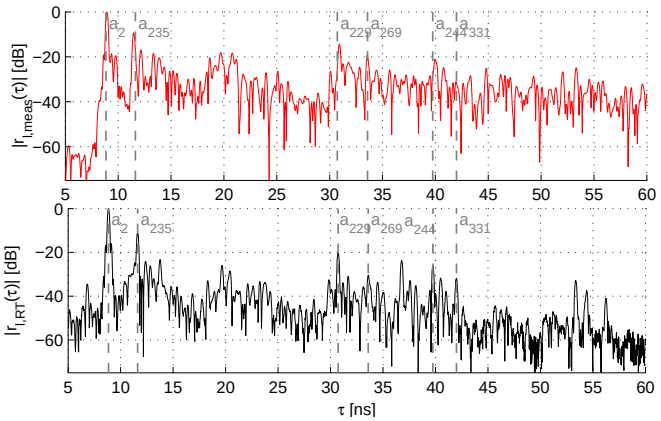

Fig. 2. Comparison of received signals obtained from measurements (top, red) and RT (bottom, black) at position $l = 11$. The dashed grey vertical lines indicate expected delays of specular MPCs at this position.

Fig. 1 also visualizes some of the predicted rays. In this work, the propagation mechanisms taken into account are: LOS, reflection (up to the third order), single diffraction, single bounce scattering, scattering-reflection and reflection-scattering cases. The penetration contribution has been embedded into all other mechanisms. It has been previously mentioned that the subdivision of surfaces in tiles for scattering interaction is related to the wavelength. More obstacles would look rougher at higher frequencies than at the lower frequencies. Therefore, the subdivision of one rough surface would be different over different sub-bands. This impacts significantly on the computational effort. Therefore, we assume, for a specific Rx's position, the subdivision of each surface at 6.85 GHz to be valid for all sub-bands. This simplified method leads to results comparable to the original one where the subdivision is changed according to the center frequency.

D. Comparison of measurement and RT signals

For comparison, the RT signals have been normalized such that the mean amplitude of their LOS path over the positions (see Fig. 1b) equals the corresponding mean of the measured signals. Fig. 2 shows signals obtained from measurements and RT at position $\mathbf{p}_{11}$, which is in the middle of the measurement grid. The grey dashed lines indicate the delays $\tau_{k,\ell}$ of some specular reflected paths modeled by the VAs. Though one can see that most of these paths are similarly present in both

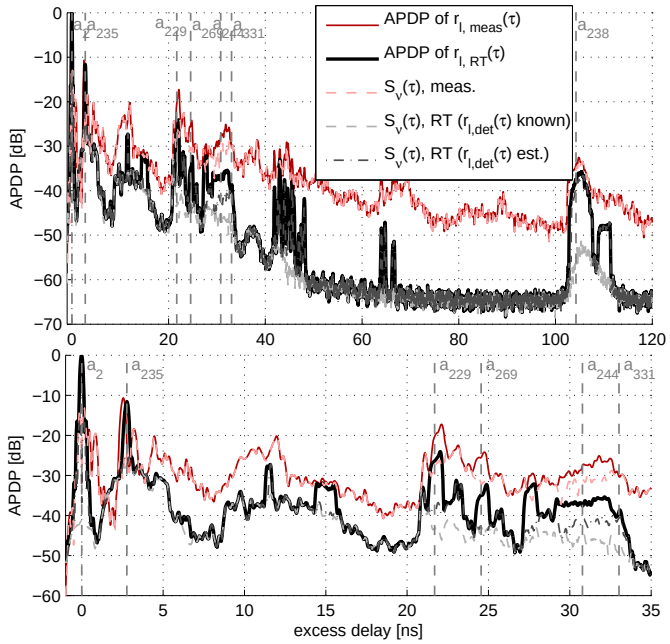

Fig. 3. Comparison of several PDPs: Solid lines denote PDPs of the overall received signal, dashed ones indicate PDPs of the DM. The lower figure provides a close-up view on the delay axis. Dashed vertical lines indicate the mean excess delay of the MPCs analyzed in Section V.

signals, the large amount of DM makes a comparison difficult.

Fig. 3 shows several PDPs, averaged over the positions where RT signals are available (see Fig. 1b). The DM and deterministic part are estimated using (2). For the RT, $S_\nu(\tau)$ can also be calculated using the available true $r_{\ell,\text{det}}(\tau)$ and $\nu_\ell(\tau)$. $S_\nu(\tau)$ without the position index ℓ indicates that the averaging is performed over all 22 RT points, i.e. the locality is eliminated. The mean excess delays of MPCs that are used for multipath-assisted localization are shown. One can see that the DM generated by RT follows the measured one qualitatively up to an excess delay of about 30 ns. The reason for the gap afterwards is that the higher order propagation mechanisms are not considered by the RT algorithm. This together with the rather large dimensions of the environment make the PDP look rather sparse after $\tau = 30$ ns. For Figs. 2, 3, and 4, the minimum usable pulse duration $T_p = 0.2$ ns with a roll-off factor of $\beta_R = 0.5$ and $f_c = 6.85$ GHz has been used.

In Fig 4, a comparison of the K-factor with respect to the LOS path K_{LOS} and the RMS delay spread τ_{RMS} between measurements and RT is shown. Due to the limited range of delays for which RT provides significant DM, K_{LOS} is considerably higher than for the measurements, also causing a lower estimate of τ_{RMS}. However, these observations still allow no direct conclusions on the influence on the localization performance, which is the focus of the next section.

IV. Estimation of Position-Related Parameters

In this Section, a more detailed analysis of the measurement and RT results, tailored to the localization application, is presented. As derived in [3], the Cramér-Rao lower bound

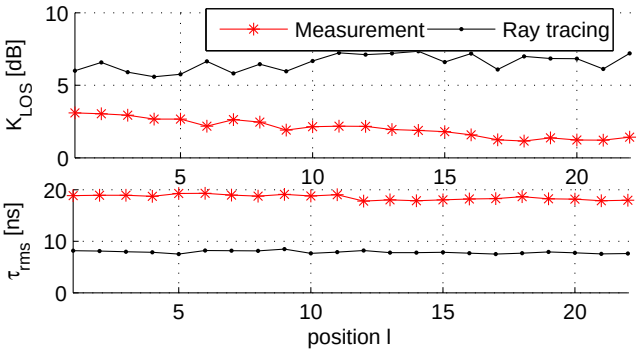

Fig. 4. K-factor with respect to the LOS component and RMS delay spread of measured (red) and RT signals (black).

on the position estimation for MINT is given as the inverse of the equivalent Fisher information matrix (EFIM) [15]

$$\mathbf{J}_{\mathbf{p}_\ell} = \frac{8\pi^2\beta^2}{c^2}\sum_{k=1}^{K_\ell} \text{SINR}_{k,\ell}\mathbf{J}_\mathbf{r}(\phi_{k,\ell}). \tag{5}$$

In (5), β denotes the effective (RMS) bandwidth of $s(\tau)$ and it is assumed that no deterministic MPCs overlap in the delay domain. The ranging direction matrix $\mathbf{J}_\mathbf{r}(\phi_{k,\ell})$ is defined as

$$\mathbf{J}_\mathbf{r}(\phi_{k,\ell}) = \begin{bmatrix} \cos^2(\phi_{k,\ell}) & \cos(\phi_{k,\ell})\sin(\phi_{k,\ell}) \\ \cos(\phi_{k,\ell})\sin(\phi_{k,\ell}) & \sin^2(\phi_{k,\ell}) \end{bmatrix}. \tag{6}$$

It indicates the geometric information contribution of the k-th MPC, as it has one eigenvector pointing in the direction $\phi_{k,\ell}$, the angle from the VA at $\mathbf{p}_k$ to position $\mathbf{p}_\ell$. This information is weighted by the $\text{SINR}_{k,\ell}$ of the k-th MPC, defined as

$$\text{SINR}_{k,\ell} = \frac{|\alpha_{k,\ell}|^2}{N_0 + T_p S_{\nu,\ell}(\tau_{k,\ell})}. \tag{7}$$

As (7) includes local (in the delay domain) effects of both the deterministic and diffuse part of the channel and determines the accuracy of multipath-assisted localization, we use it to evaluate the suitability of RT for performance prediction, i.e. the computation of the CRLB for a geometrically given environment. We observe that the estimation of the SINRs depends to a great extent on the level of channel knowledge, i.e. the availability of the local PDP of the DM $S_{\nu,\ell}(\tau)$.

A. Estimation of the instantaneous $\text{SINR}_{k,\ell}$ – PDP available

The availability of grid measurements allow for a local PDP estimation $\hat{S}_{\nu,\ell}(\tau)$ using (2) and (3). For RT, the provided channel decomposition into deterministic MPCs and DM enables the calculation of the "true" $S_\nu(\tau)$, which is used for all RT positions. With this and estimated path amplitudes as described in the previous section, a direct evaluation of (7), i.e. an estimate $\widehat{\text{SINR}}_{k,\ell}$, is possible. We expect that the RT can provide good ground-truth values for this, while for the measurements, $\widehat{\text{SINR}}_{k,\ell}$ will depend crucially on the local PDP estimate $\hat{S}_{\nu,\ell}(\tau)$.

For the evaluation of the PDP of the DM for a certain excess delay $\tau_{k,\ell}$ in (7), not only $\hat{S}_{\nu,\ell}(\tau_{k,\ell})$, but the local mean value

of this PDP within one T_p is chosen. This is done to avoid errors due to artifacts caused by the MPC subtraction in (2). The noise power N_0 is estimated from the pre-LOS portion of the measured signals. To allow for a fair comparison, this quantity is then also used for the SINR estimation of the RT signals, as these do not contain measurement noise.

B. Estimation of the average SINR$_k$ – PDP not available

If densely spaced grid measurements are not available, the local PDP of the DM can not be estimated reliably. Therefore, measurements within some local area, e.g. at M points along a route, have to be combined statistically. This renders the estimation of the instantaneous SINR$_{k,\ell}$ impossible, and gives rise to an average SINR$_k$. The estimation of this SINR$_k$ is described in detail in [2], and just shortly re-sketched here. Using the delay $\tilde{\tau}_{k,\ell}$ calculated from geometry, the received signal is projected onto a unit energy template pulse $s(\tau)$

$$\hat{\alpha}_{k,\ell} = \int_0^T r_\ell(\tau) s^*(\tau - \tilde{\tau}_{k,\ell}) d\tau \tag{8}$$

where T is the observation time. Under the assumptions that no path overlap between the k-th and any other MPC occurs, that $\tilde{\tau}_{k,\ell} = \tau_{k,\ell}$, and that $s(\tau) \approx 0$ for $|\tau| > T_p$, this reduces to $\hat{\alpha}_{k,\ell} = \alpha_{k,\ell} + \nu_{k,\ell} + w_{k,\ell}$. This is a superposition of the deterministic MPC amplitude and noise. If both $\nu_\ell(\tau)$ and $w_\ell(\tau)$ are Gaussian processes, $\hat{\alpha}_{k,\ell}$ follows a Ricean distribution and the energy samples $|\hat{\alpha}|^2_{k,\ell}$ follow a non-central χ^2-distribution with two degrees of freedom. Based on the sample mean and variance of $|\hat{\alpha}|^2_{k,\ell}$, denoted as m_{1,α_k^2} and m_{2,α_k^2}, estimated over the M considered positions, an estimator of SINR$_k$ has been derived as

$$\widehat{\text{SINR}}_k = \left(\frac{m_{1,\alpha_k^2}}{\sqrt{m_{1,\alpha_k^2}^2 - m_{2,\alpha_k^2}}} - 1 \right)^{-1}. \tag{9}$$

For this, two additional steps need to be performed. First, as the geometry is not known perfectly, the delays $\tilde{\tau}_{k,\ell}$ have to be re-estimated. This is done using a maximum-likelihood (ML) re-localization of the VAs over the M considered points. Second, any variations in $\hat{\alpha}_{k,\ell}$ are inherently attributed to the DM by this estimator. Hence, the estimated amplitudes are corrected by a path-loss factor accounting for the deterministic dependence on the varying distance to the Tx. These procedures are described in detail in [2].

Finally, we note that if the true $S_{\nu,\ell}(\tau)$ was used for the estimation of the instantaneous SINR$_{k,\ell}$ using (7), then $\widehat{\text{SINR}}_k \approx \frac{1}{M}\sum_\ell \widehat{\text{SINR}}_{k,\ell}$, i.e. evaluated over the same positions, both averages should be equal. The right hand side of this expression is used in performance results where it is called average $\widehat{\text{SINR}}_{k,\ell}$, indicating the difference to (9).

V. Results

For the evaluation of the SINR estimation techniques, we selected different exemplary bandwidths and frequency bands from measurement and RT signals. This was done using the pulse shaping approach described in Section II with different pulse durations T_p of the raised-cosine pulse and different center frequencies f_c. The filtered signals were converted to complex baseband. Because of the restriction of the DM to excess delays smaller than 30 ns explained in Section III-D, we restrict the analysis to those deterministic MPCs within this range of delays, except for the VA at $\mathbf{a}_{238}$, which is the reflection at the far right wall of the corridor shown in Fig. 1b. For the measurements, the local PDP of the DM is estimated for every point $\mathbf{p}_\ell$ using (3), where the $L = 15$ spatially closest points are taken into account, while for the RT, the available true $S_\nu(\tau)$ over all 22 points is used.

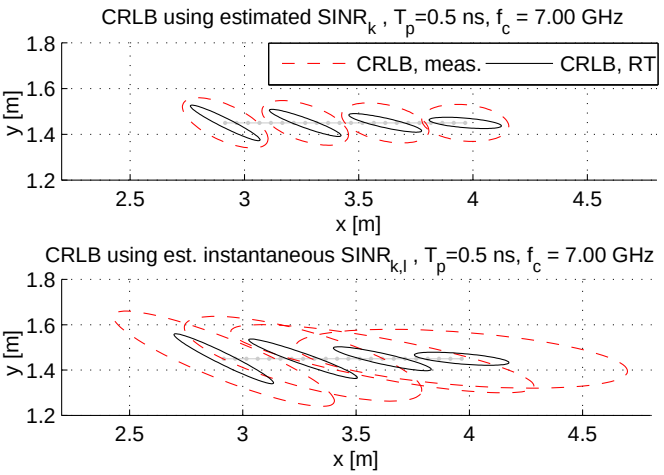

Fig. 5. Standard deviation ellipses for the CRLB over selected positions, enlarged by a factor of 30, to ease perceptibility. Upper plot shows the CRLB using the SINR estimate (9), lower plot uses the instantaneous estimate $\widehat{\text{SINR}}_{k,\ell}$ for the corresponding position. Red dashed ellipses denote results using measured data, for the black ellipses, ray tracing simulations were used.

Table I shows a comparison of the obtained SINR estimates for different pulse parameters. We notice that although some MPCs match well, many SINR estimates are quite different for RT and measurements. This has several reasons, where one is that measurement data shows much more variance than the deterministically generated RT data. For example, the most obvious discrepancy occurs for the SINR of the LOS path. This is caused by the antenna pattern of the Rx in the measurements, which deviates by a few dB from omnidirectionality. An unfortunate orientation of the antennas caused the LOS amplitude to decrease when moving towards the Tx along the grid. This additional variation in the LOS amplitude is considered as DM by the SINR estimation. Also, RT does not consider any scattering in the immediate surroundings of the antenna, i.e. platform effects, which leads to an underestimation of DM around zero excess delay. The importance of modeling the frequency dependence of material properties is shown e.g. by VA 235, which models the pillar above the Tx. At $T_p = 0.5$ ns, we observe a much higher SINR in the measurements at $f_c = 7$ GHz than at $f_c = 9$ GHz, which is not predicted by the RT.

Additional insights in the estimators can be obtained from VA 238, modeling the reflection on the far right wall. For

TABLE I

SINRs FOR DIFFERENT T_p AND f_c. IN EACH CASE, RESULTS ARE SHOWN BOTH FOR MEASURED SIGNALS AND RT SIMULATIONS. ESTIMATES FOR THE MEAN SINR_k AND THE INSTANTANEOUS $\text{SINR}_{k,l}$ ARE SHOWN. SR, DR AND TR DENOTE SINGLE-, DOUBLE AND TRIPLE REFLECTION, RESPECTIVELY.

MPC		T_p =0.2 ns, f_c =6.85 GHz		T_p =0.5 ns, f_c =7 GHz		T_p =0.5 ns, f_c =9 GHz	
Index (description)	mean exc. delay [ns]	$\widehat{\text{SINR}}_k$ [dB] Meas./RT	avg. $\widehat{\text{SINR}}_{k,\ell}$ [dB] Meas./RT	$\widehat{\text{SINR}}_k$ [dB] Meas./RT	avg. $\widehat{\text{SINR}}_{k,\ell}$ [dB] Meas./RT	$\widehat{\text{SINR}}_k$ [dB] Meas./RT	avg. $\widehat{\text{SINR}}_{k,\ell}$ [dB] Meas./RT
2 (LOS)	8.96	17.7 / 40.4	16.6 / 40.9	16.8 / 39.0	18.7 / 37.7	12.8 / 37.8	12.1 / 37.0
229 (SR, lower wind.)	30.66	18.6 / 23.2	13.6 / 23.6	14.5 / 18.1	12.8 / 18.7	13.4 / 19.7	8.5 / 19.1
235 (SR, pillar)	11.74	26.6 / 17.4	19.7 / 16.5	26.8 / 14.0	24.0 / 13.4	17.0 / 12.2	16.0 / 13.9
238 (SR, right wall)	113.2	21.0 / 24.1	6.5 / 23.1	19.9 / 21.2	6.4 / 17.1	19.5 / 14.6	7.5 / 15.0
244 (DR, lower-left)	39.7	10.4 / 18.9	11.9 / 19.7	7.6 / 15.4	11.8 / 16.4	3.0 / 14.5	9.9 / 14.1
269 (DR, pillar-wind.)	33.5	10.5 / 14.1	11.0 / 14.9	8.0 / 10.5	11.0 / 10.9	6.0 / 10.0	10.4 / 11.6
331 (TR, corner-pillar)	42.0	3.9 / 14.1	6.7 / 13.2	5.8 / 10.0	6.3 / 7.9	-∞/12.7	0.2 / 7.6

this, the two SINR estimators differ significantly using the measurements. The right wall is modeled as a single surface, while in reality, it is a more complex structure causing a diffuse cluster. Because this cluster has quite homogeneous amplitude characteristics, $\widehat{\text{SINR}}_k$ according to (9) is large. But as can be seen from Fig. 3, the diffuse cluster is very significant in $S_\nu(\tau)$. This channel knowledge is used by $\widehat{\text{SINR}}_{k,\ell}$, thus reflecting the MPC behavior better. We further note that $\widehat{\text{SINR}}_k$ and $\widehat{\text{SINR}}_{k,\ell}$ obtained by RT and therefore the exact $S_\nu(\tau)$ match very well, which validates (9) as estimator for the mean SINR of an MPC.

Fig. 5 shows standard deviation ellipses given by the CRLB as inverse of the EFIM in (5) for $T_p = 0.5\,\text{ns}$ and a center frequency of $f_c = 7\,\text{GHz}$. The ellipses are enlarged by a factor of 30 to allow for easier perceptibility. Despite the fact that there are considerable differences in the numeric values of the SINR between measurements and RT, the obtained error ellipses, especially for the mean SINR_k, seem reasonable for performance prediction. Although the basic orientation of the ellipses is given by the geometry and is the same for measurements and RT, the different SINRs do not cause a change of this orientation. The most obvious deviation seems to be in the direction to the physical anchor, as the LOS path shows the largest error in terms of the SINR estimation.

VI. CONCLUSIONS AND OUTLOOK

In this paper, the use of RT for the application of indoor localization has been discussed. We have highlighted the importance of the diffuse multipath for performance prediction and used a sub-band divided RT tool that is capable of modeling scattered signal paths. In this stage of development, there are still considerable differences in estimated localization performance parameters between measurements and RT. However, the obtained results for the CRLB on the position accuracy seem to show general agreement. This makes it conceivable to replace time-consuming measurements campaigns by offline RT simulations before installing an indoor localization system.

Future work could include a calibration technique for the RT using some limited channel measurements. This could alleviate the need for detailed knowledge of the electrical parameters of the building materials over a large frequency range.

REFERENCES

[1] N. Alsindi, B. Alavi, and K. Pahlavan, "Measurement and Modeling of Ultrawideband TOA-Based Ranging in Indoor Multipath Environments," *Vehicular Technology, IEEE Transactions on*, vol. 58, no. 3, pp. 1046 –1058, Mar. 2009.

[2] P. Meissner and K. Witrisal, "Analysis of Position-Related Information in Measured UWB Indoor Channels," in *6th European Conference on Antennas and Propagation (EuCAP)*, Prague, Czech Repuplic, 2012.

[3] K. Witrisal and P. Meissner, "Performance Bounds for Multipath-aided Indoor Navigation and Tracking (MINT)," in *International Conference on Communications (ICC)*, Ottawa, Canada, 2012.

[4] Y. Shen and M. Win, "On the Use of Multipath Geometry for Wideband Cooperative Localization," in *Global Telecommunications Conference, 2009. GLOBECOM 2009. IEEE*, 2009, pp. 1 – 6.

[5] G. Tiberi, S. Bertini, W. Malik, A. Monorchio, D. Edwards, and G. Manara, "Analysis of Realistic Ultrawideband Indoor Communication Channels by Using an Efficient Ray-Tracing Based Method," *Antennas and Propagation, IEEE Transactions on*, vol. 57, no. 3, pp. 777 – 785, Mar. 2009.

[6] T. Santos, F. Tufvesson, and A. Molisch, "Modeling the Ultra-Wideband Outdoor Channel: Model Specification and Validation," *Wireless Communications, IEEE Transactions on*, vol. 9, no. 6, pp. 1987 –1997, 2010.

[7] H. Sugahara, Y. Watanabe, T. Ono, K. Okanoue, and S. Yarnazaki, "Development and experimental evaluations of "RS-2000" - a propagation simulator for UWB systems," in *Ultra Wideband Systems, 2004. Joint with Conference on Ultrawideband Systems and Technologies*, May 2004, pp. 76 – 80.

[8] J. Jemai, P. Eggers, G. Pedersen, and T. Kürner, "On the Applicability of Deterministic Modelling to Indoor UWB Channels," in *3rd Workshop on Positioning, Navigation and Communication (WPNC'06)*, 2006.

[9] S. U. Inan and S. A. Inan, *Electromagnetic Waves*. Prentice Hall, 2000.

[10] R. Luebbers, "Finite conductivity uniform GTD versus knife edge diffraction in prediction of propagation path loss," *Antennas and Propagation, IEEE Transactions on*, vol. 32, no. 1, pp. 70 – 76, Jan. 1984.

[11] F. Mani, F. Quitin, and C. Oestges, "Accuracy of depolarization and delay spread predictions using advanced ray-based modeling in indoor scenarios," *EURASIP Jounal in Wireless Commmunications and Networking*, vol. 2011, p. 11, 2011.

[12] V. Degli-Esposti, F. Fuschini, E. M. Vitucci, and G. Falciasecca, "Measurement and Modelling of Scattering From Buildings," *Antennas and Propagation, IEEE Transactions on*, vol. 55, no. 1, pp. 143 – 153, Jan. 2007.

[13] F. Mani, F. Quitin, and C. Oestges, "Directional Spreads of Dense Multipath Components in Indoor Environments: Experimental Validation of a Ray-Tracing Approach," *Antennas and Propagation, IEEE Transactions on*, vol. 60, no. 7, pp. 3389 – 3396, July 2012.

[14] Y. Zhao, Y. Hao, A. Alomainy, and C. Parini, "UWB on-body radio channel modeling using ray theory and subband FDTD method," *Microwave Theory and Techniques, IEEE Transactions on*, vol. 54, no. 4, pp. 1827 – 1835, June 2006.

[15] Y. Shen and M. Win, "Fundamental Limits of Wideband Localization - Part I: A General Framework," *Information Theory, IEEE Transactions on*, vol. 56, no. 10, pp. 4956 –4980, 2010.